

# A Preliminary Attempt on Decadal Prediction of the East Asian Summer Monsoon

Danwei Qian (✉ [qiandw12@126.com](mailto:qiandw12@126.com))

Nanjing University of Information Science and Technology <https://orcid.org/0000-0002-0854-2248>

Yanyan Huang

Nanjing University of Information Science and Technology <https://orcid.org/0000-0003-2621-0826>

Huijun Wang

Nanjing University of Information Science and Technology

---

## Research Article

**Keywords:** East Asian summer monsoon, Decadal prediction, Decadal increment method

**Posted Date:** November 16th, 2021

**DOI:** <https://doi.org/10.21203/rs.3.rs-697966/v2>

**License:** © ⓘ This work is licensed under a Creative Commons Attribution 4.0 International License.

[Read Full License](#)

---

**Version of Record:** A version of this preprint was published at Theoretical and Applied Climatology on March 18th, 2022. See the published version at <https://doi.org/10.1007/s00704-022-04011-w>.



15 **ABSTRACT**

16 The East Asian summer monsoon (EASM) is one of the major synoptic systems that affect  
17 the summer climate in China. Decadal prediction of the EASM is of great significance, yet few  
18 attempts have been made by far. This study represents a preliminary attempt that uses the  
19 decadal increment (DI) method to predict the decadal variability of the EASM. The 3-year  
20 increment of the decadal variability is used as the predictand, and predictors are selected from  
21 the previous circulation and external forcing. The predicted increment is combined with the  
22 observation three years ago to get the final prediction result. The results of cross validation and  
23 independent hindcast show that the decadal increment method can well predict decadal  
24 variability of the EASM during the recent century. In particular, the decadal regime shifts of  
25 the EASM are accurately captured. The decadal variability of the EASM in 2021 is further  
26 predicted with two previous predictors of the leading 4-year summer DI of the South Indian  
27 Ocean and the DI of the East Siberian Sea sea ice cover. The real-time prediction results show  
28 that the chance for the occurrence of strong decadal EASM would be rare in 2021 and 2022.  
29 The method developed in the present study provides a new approach for decadal prediction of  
30 the EASM.

31 **Keywords** East Asian summer monsoon; Decadal prediction; Decadal increment method  
32

## 33 **Declarations**

### 34 *Funding*

35 This research was funded by the National Natural Science Foundation of China [grant  
36 number 41991283, 42088101, 42025502].

### 37 *Availability of data and material*

38 Sea ice concentration data from the Met Office Hadley are available at  
39 <https://www.metoffice.gov.uk/hadobs/hadisst/data/download.html>; The National Oceanic and  
40 Atmospheric Administration (NOAA) Extended Reconstructed SST v3b dataset are from  
41 <https://psl.noaa.gov/data/gridded/data.noaa.ersst.v3.html>; The fifth generation European  
42 Centre for Medium-Range Weather Forecasts (ECMWF) atmospheric reanalysis (ERA5)  
43 are obtained at <https://www.ecmwf.int/en/forecasts/dataset/ecmwf-reanalysis-v5>. The  
44 Twentieth Century Reanalysis Product v3 dataset can be downloaded at  
45 [https://psl.noaa.gov/data/gridded/data.20thC\\_ReanV3.pressure.html](https://psl.noaa.gov/data/gridded/data.20thC_ReanV3.pressure.html).

### 46 *Code availability*

47 All the codes are programmed by NCAR Command Language. The codes are available and  
48 maintained by author.

### 49 *Conflicts of interest /Competing interests*

50 The authors declare no conflicts of interest or competing interests.

### 51 *Authors' contributions*

52 Conceptualization: D.W.Q., Y.Y.H. and H.J.W.; Methodology: Y.Y.H. and H.J.W.; Formal  
53 analysis and software: D.W.Q.; Writing - original draft preparation: D.W.Q.; Writing - review  
54 and editing: D.W.Q., Y.Y.H. and H.J.W. All authors have read and agreed to the published  
55 version of the manuscript.

56

## 57 **1. Introduction**

58       The East Asian summer monsoon (EASM) refers to the southerly winds that prevail in East  
59 Asia in summer. As a unique component of the Asian climate system, the EASM demonstrates  
60 special spatiotemporal structure and dominates climate and climate change in East Asia (Tao  
61 et al. 1987; Ding et al. 1994; Huang et al. 2004). Due to its interactions with the climate system  
62 on multiple time scales, the EASM shows large variations from intraseasonal to interdecadal  
63 scale. The interaction between the EASM and the climate system often leads to anomalies of  
64 the EASM, which can subsequently cause heavy droughts and floods in China. Such kinds of  
65 meteorological disasters impose serious impacts on people's lives and economic activities in  
66 East Asia. Therefore, reliable prediction of the EASM changes is of great significance (Huang  
67 et al. 2007; Ha et al. 2012). On the intraseasonal scale, the EASM often demonstrates 10–20-  
68 day and 30–60-day oscillation patterns (Chen et al. 2001; Mao and Chan 2005; Guan and  
69 Johnny 2006). On the interannual scale, 2-year and 4-year oscillations account for a large part  
70 of the EASM variability. These intraseasonal and interannual variabilities of the EASM have  
71 remarkable impacts on summer rainfall in China and large-scale circulation in East Asia (Meehl  
72 and Arblaster 2002; Wu et al. 2008; Ding et al. 2013). Decadal climate change is defined as  
73 changes on the time scale of 10–30 year in the future. In the 20th century, the EASM has  
74 undergone significant decadal changes. The weakening of the EASM that occurred at the end  
75 of the 1970s (Wang 2001; Xue 2001; Wang 2002; Huang et al. 2004; Ding et al. 2008) was  
76 characterized by weaker than normal south-westerly winds in the surface level and at 850hPa  
77 and a weakened easterly jet in the upper troposphere (Hu 1997; Xu et al. 2006; Ding et al.  
78 2008; Zhou et al. 2009). Meanwhile, the western Pacific subtropical high retreated to the east  
79 (Huang et al. 2015; Huang and Li 2015; Tong et al. 2020). At the beginning of the 1990s, the  
80 EASM started to intensify (Liu et al. 2012; Ding et al. 2013).

81 Corresponding to the aforementioned decadal changes in the EASM, summer precipitation  
82 in China has also experienced significant decadal changes. From the middle of the 1960s to the  
83 end of the 1970s, the rain belts in eastern China were located in North China and South China,  
84 while the Jianghuai and Yangtze river basins had less than normal precipitation. The spatial  
85 distribution of rainfall anomaly displayed a “positive-negative-positive” pattern (“+ - +”  
86 meridional pattern) along the meridional direction. In the late 1970s, following the EASM  
87 weakening, the rainfall zone shifted to the Yangtze River basin, while precipitation in North  
88 China and South China decreased. Precipitation anomaly presented a “negative-positive-  
89 negative” pattern (“- + -” pattern) along the meridional direction. By the early 1990s, with the  
90 intensification of the summer monsoon, the main rainfall zone moved northward again, and a  
91 dipole-type of rainfall pattern prevailed in eastern China with floods in the north and droughts  
92 in the south (Wang 2001; Ding et al. 2008; Si et al. 2009; Zhu et al. 2010; Huang et al. 2011;  
93 Lü et al. 2014; Ding et al. 2018).

94 Many scientists have conducted research to explore the mechanisms for the decadal  
95 variability of the EASM. At the end of the 1970s, it was found that a persistent interdecadal  
96 scale cooling occurred in the upper troposphere and lower stratosphere. On the one hand, it  
97 affected the cyclonic circulation anomaly in the upper levels and promoted the strengthening  
98 of the westerly winds to the south of the East Asian jet axis. On the other hand, it influenced  
99 the anticyclonic circulation anomaly in the lower levels and weakened the EASM (Yu et al.  
100 2004, 2007). Based on results of numerical experiments, Li et al. (2008) demonstrated that the  
101 decadal weakening of the EASM is attributed to the decadal change in the tropical sea surface  
102 temperature (SST). Changes in the SST over the tropical central and eastern Pacific led to  
103 tropospheric warming above the tropical ocean in the late 1970s. At the same time, temperature  
104 in the temperate zone of continental East Asia decreased. As a result, the thermal contrast  
105 between the ocean and the land reduced, which subsequently weakened the EASM. Yu (2013)

106 believed that the negative correlation between the phases of the Pacific Decadal Oscillation  
107 (PDO) and the EASM is the reason for the decadal weakening of the EASM since the late  
108 1970s. The phase change of the PDO caused SST variation in the Pacific and Indian oceans,  
109 which affected the intensity of the western Pacific subtropical high and led to the anticyclone  
110 anomaly over the western Pacific. As a result, the EASM was weakened (Gong and Ho 2002;  
111 Dong and Xue 2016). In addition, Ding et al. (2008, 2009) found that the weakening of the  
112 atmospheric heating over the Tibet Plateau since the late 1970s has effectively reduced sensible  
113 heat flux transfer from the surface to the atmosphere, leading to increased snowfall in the  
114 previous winter and spring. Larger than normal snow cover in the Tibet Plateau delayed the  
115 formation of monsoon temperature gradient, and thereby weakened the EASM. Other factors  
116 such as North Atlantic SST tripole and North Pacific Gyre Oscillation can also affect the  
117 decadal variability of the EASM (Zuo et al. 2013; Ye et al. 2016).

118 In recent years, extensive attention has been focused on decadal climate prediction, which  
119 potentially has great impacts on economic and social development (Meehl et al. 2014; Zhou et  
120 al. 2017). Decadal climate prediction at present mainly relies on the initialized climate models,  
121 yet the initial shock is still a problem in the model initialization that hasn't been fully solved  
122 (Meehl et al. 2014; Zhou et al. 2017). Compared with that in the North Pacific, the initialization  
123 in decadal prediction over the North Atlantic has been remarkably improved (Doblas-Reyes et  
124 al. 2013; Kirtman et al. 2013). Most of the current models have demonstrated satisfactory skills  
125 for prediction of the Atlantic Multidecadal Oscillation, whereas the model skills for PDO  
126 prediction are generally low (Kim et al. 2012). In addition, the model performance for the  
127 prediction of land surface temperature in the northern hemisphere remains poor. Compared  
128 with the uninitialized prediction skills, the model performance shows no obvious improvement  
129 after implementing initialization strategies (Doblas-Reyes et al. 2013; Wu et al. 2019). Also,  
130 decadal prediction of precipitation by climate models still has problems. The models only show

131 prediction skills over some areas, and the improvements are quite limited even after the  
132 initialization strategy is implemented (Kirtman et al. 2013; Meehl et al. 2014; Wang et al.  
133 2018). Therefore, decadal climate prediction by current climate models still remains a  
134 challenging issue.

135 Based on the interannual increment approach (Fan et al. 2008; Wang et al. 2012), Huang  
136 and Wang (2020a, b) proposed a decadal increment method to address climate prediction. In  
137 this method, decadal signals are first obtained from moving averages of the raw data, and the  
138 decadal increments are then used to identify the predictors to build the forecast model. Finally,  
139 the predicted increment is combined with the previous observations to get the final prediction  
140 result. This method helps to increase the effective samples and obtain more useful decadal  
141 signals of the climate system from previous observations. Great progress has been made in the  
142 predictions of PDO and decadal variability of summer precipitation in North China using the  
143 decadal increment method. However, it still remains questionable whether this method can be  
144 effectively applied to the prediction of other climate variables. Taking into account the close  
145 relationship between the EASM and the summer climate in China and the limited predictive  
146 skills of current climate models for precipitation and land surface temperature, this study  
147 attempts to predict decadal variability of the EASM using the decadal increment method.

148 The rest of this article is organized as follows. Section 2 describes the datasets and method.  
149 Section 3 introduces how to use the decadal increment to build a statistical model. The hindcast  
150 skills of the statistical model based on the decadal incremental method are presented in Section  
151 4. Section 5 uses this method to build a real-time prediction model to predict EASM. The  
152 discussion is given in Section 6. Finally, Section 7 presents the summary.

## 153 **2. Data and methods**

154 Monthly mean reanalysis datasets used in this study include the following:

155 1) Horizontal wind components (U and V) and geopotential height are extracted from the  
156 Twentieth Century Reanalysis Product v3 (20CR) with a horizontal resolution of  $1^\circ \times 1^\circ$  and  
157 cover the period from 1910–2012 (Compo et al. 2011);

158 2) Sea surface temperature (SST) data with a horizontal resolution of  $2^\circ \times 2^\circ$  are from the  
159 National Oceanic and Atmospheric Administration (NOAA) Extended Reconstructed SST v3b  
160 dataset and covers the period from 1910–2012 (Smith et al. 2008);

161 3) Sea ice cover (SIC) data are from the Met Office Hadley Centre with a horizontal resolution  
162 of  $1^\circ \times 1^\circ$  and covers the period from 1910–2012 (Rayner et al. 2003).

163 4) Horizontal wind components (U and V), sea surface temperature (SST) and sea ice cover  
164 (SIC) are derived from the fifth generation European Centre for Medium-Range Weather  
165 Forecasts (ECMWF) atmospheric reanalysis (ERA5, Hersbach et al. 2020) with a horizontal  
166 resolution of  $1^\circ \times 1^\circ$  and cover the period from 1980–2020.

167 The first three datasets have been chosen to calculate the EASMI in sections 3, 4 and 6, and  
168 the last dataset has been used in section 5.

169 The EASM index (EASMI) is defined as the area-mean ( $110\text{--}125^\circ\text{E}$ ,  $20^\circ\text{N}\text{--}40^\circ\text{N}$ ) wind  
170 speed at 850hPa in summer (June–July–August) (Wang 2002). Based on the decadal increment  
171 method proposed by Huang and Wang (2020a, b), the statistical model is established. First,  
172 decadal EASMI is obtained from the 5-year running mean of the original EASMI and marked  
173 as EASMI in the middle year of the five years. Decadal increment (DI) of the EASMI  
174 (DI\_EASMI) is then calculated from decadal EASMI, that is, the decadal EASMI of the current  
175 year minus the decadal EASMI three years ago will be treated as DI\_EASMI of the current  
176 year (Eq. 1). Finally, predictors are identified based on DI\_EASMI and a prediction model is  
177 built using these predictors. The final predicted EASMI is the predicted DI\_EASMI plus the  
178 observed EASMI three years ago (Eq. 2). For example, the final predicted EASMI in 1924 is

179 obtained by adding the predicted DI\_EASMI in 1924 to the observed EASMI in 1921. Similar  
 180 to the DI of the predictand, the DI of the predictor is obtained by performing the 5-year running  
 181 mean first and then calculating the 3-year increment. To avoid possible containing of the  
 182 information of the prediction period in the predictors, the predictors have to lead the predictand  
 183 by at least three years. For example, the summer DI of the SST (DI\_SST) from 1918 to 2007  
 184 and the DI\_EASMI from 1921 to 2010 are used for correlation analysis to find key predictors,  
 185 and so on.

$$186 \quad DI\_EASMI_i = EASMI_i - EASMI_{i-3} \quad (1)$$

$$187 \quad EASMI_i = EASMI_{i-3}^{obs} + DI\_EASMI_i^{pre} \quad (2)$$

188 In order to judge whether climate variables follow normal distribution, the skewness  
 189 coefficient (g1) and kurtosis coefficient (g2) are calculated.

$$190 \quad g1 = \sqrt{\frac{1}{6n}} \sum_{i=1}^n \left( \frac{x_i - \bar{x}}{s} \right)^3 \quad (3)$$

$$191 \quad g2 = \sqrt{\frac{n}{24}} \left[ \frac{1}{n} \sum_{i=1}^n \left( \frac{x_i - \bar{x}}{s} \right)^4 - 3 \right] \quad (4)$$

192 Where n is the number of the sample,  $\bar{x}$  and s are the mean and standard deviation of the  
 193 sample. The skewness coefficient characterizes the degree to which the peak of the curve  
 194 deviates from the mean value. A positive g1 indicates that the mean is to the left of the peak,  
 195 and a negative g1 indicates that the mean is to the right of the peak. The kurtosis coefficient  
 196 characterizes the convexity of the peak of the distribution pattern and measures the degree of  
 197 concentration of the frequency distribution. A positive g2 indicates that the frequency  
 198 distribution is more concentrated than the normal distribution, and the average is more  
 199 representative, and a negative g2 is the opposite.

200 Cross validation and independent hindcast are used to verify the predictive skill of the  
 201 established empirical statistical model. In the cross validation, the EASM observational data  
 202 for the period 1921–2010 and the predicted EASM data three/four/five years ahead of the  
 203 observation time are selected first, and the 5-year data centred on the target year are excluded.  
 204 The data in the remaining years are then used to build the model to predict the EASM in the  
 205 target year. This process is repeated for each target year. The first and last three years of the  
 206 data are verified by leaving the first and last five years of data out. The independent hindcast  
 207 uses the same observational data. To avoid using the information of the prediction period, the  
 208 data from the starting year to three years ahead of the target year are used as the training  
 209 samples to establish the empirical statistical model to predict the situation in the target year.  
 210 The aforementioned process is repeated for 1980–2010. For example, if the target year is 1990  
 211 (1991), the data from 1921–1987 (1921–1988) is used to build the prediction model.

212 The moving t-test (MTT) with a 10-year moving window is used to detect regime  
 213 transitions of decadal variation of the EASM, and the significance of the correlation coefficient  
 214 is tested by Student’s t-test. The effective sample size  $N^*$  is computed (Bretherton et al. 1999):

$$215 \quad N^* = N \frac{1 - r_x r_y}{1 + r_x r_y} \quad (5)$$

216 Where  $N$  is the number of available time steps, and  $r_x$  and  $r_y$  are the autocorrelation coefficients  
 217 of the two correlated variables lagging one step behind.

218 The mean square skill score (MSSS) is used to test the predictive skill of the model  
 219 (Murphy, 1988; Goddard et al. 2012). The MSSS algorithm is written as:

$$220 \quad MSSS = 1 - \frac{MSE}{MSE_C} \quad (6)$$

$$221 \quad MSE = \frac{1}{n} \sum_{i=1}^n (f_i - o_i)^2 \quad (7)$$

222 
$$MSE_C = \frac{1}{n} \sum_{i=1}^n (o_i - \bar{o})^2 \quad (8)$$

223 Where  $f_i$  and  $o_i$  represent the time series of observations and forecasts, respectively. MSSS  
224 reflects the percentage reduction of the mean square error (MSE) predicted by the statistical  
225 model, and  $MSE_C$  is the MSE of the "climatological forecast". A positive MSSS indicates that  
226 the statistical model prediction is better than that of the "climatological forecast", and a  
227 negative MSSS indicates that the model forecast is inferior to the "climatological forecast".

### 228 **3. Prediction model**

229 Based on the definition of the EASMI, decadal EASMI is calculated. The time series of  
230 EASMI for the period 1918–2010 is displayed in Fig. 1a, which shows that the EASM was in  
231 a positive phase from 1920 to the mid-1930s and then switched to a negative phase from the  
232 mid-1930s to the mid-1940s. The EASM was relatively strong during the period from the 1950s  
233 to the 1970s, but it suddenly weakened at the end of the 1970s. This result is consistent with  
234 studies of Wang (2001), Guo et al. (2003), Huang et al. (2004) and Ding et al. (2008). In the  
235 early 1990s, the EASM began to intensify again. This phenomenon is also found in Liu et al.  
236 (2012) and Ding et al. (2013).

237 The basic assumption of climate statistics analysis is that the climate variables follow a  
238 normal distribution. When the skewness coefficient ( $g_1$ ) and kurtosis coefficient ( $g_2$ ) of the  
239 data are both less than 1.96, the data can be treated as following normal distribution at the 95%  
240 confidence level. For the decadal EASMI (Fig. 2), both the skewness coefficient and the  
241 kurtosis coefficient are higher than 1.96, which means right shifting skewness distribution than  
242 normal distribution and steeper kurtosis distribution. The 1-year and 2-year increments of  
243 decadal EASMI are also not satisfy the normal distribution. Interestingly, the 3-year increment

244 follows normal distribution at the 95% confidence level (Fig. 2). Therefore, the 3-year  
245 increment is selected for further analysis. Time series of 3-year increment is shown in Fig. 1b.

246 This paper implements the decadal increment method and uses the predictors in the decadal  
247 increment form to establish the empirical statistical model for DI\_EASMI prediction. First,  
248 based on findings of previous studies, potential predictors are identified from SST, SIC and  
249 circulation fields, etc. To avoid possible containing of the information during the prediction  
250 period in the predictors, the predictors need to lead the DI\_EASMI by at least three years. The  
251 stepwise regression method is then used to select the predictors that are significantly related to  
252 DI\_EASMI and are independent of each other. The finally built prediction model is expressed  
253 by:

$$254 \quad DI\_EASMI = 0.50 * DI\_SSTI + 0.41 * DI\_BH + 0.30 * DI\_SIC \quad (9)$$

255 the DI of the sea surface temperature index (DI\_SSTI), the DI of the Bonin high (DI\_BH) and  
256 the DI of the sea ice cover (DI\_SIC) explain 25%, 17%, and 9% of the DI\_EASMI variance,  
257 respectively.

258 The first predictor selected in this paper is the tropical ocean temperature signal in summer  
259 that leads DI\_EASMI by three years. Fig. 3a shows the spatial pattern of the correlation  
260 coefficient between DI\_SST and DI\_EASMI for the period 1921–2010. The colder equatorial  
261 western Pacific and the warmer equatorial central and eastern Pacific are conducive to the  
262 enhancement of DI\_EASMI. Physically, the equatorial central and eastern Pacific warming is  
263 favorable for the EASM intensification because anomalous ascending motions develop above  
264 the equatorial central-eastern Pacific while descending motions occur over the subtropical  
265 western Pacific. The above circulation is the so-called “quasi-Walker circulation” (Ying and  
266 Sun 2000; Wu et al. 2003; He et al. 2015). Additionally, the western Pacific cooling can  
267 strengthen the EASM through changing in-situ precipitation and further triggering descending  
268 atmospheric Rossby waves (Zhang et al. 1999; Wang et al. 2000; Wang et al. 2013; Huang et

269 al. 2018). To quantify this characteristic relationship, area-weighted regionally averaged  
270 DI\_SST in these two regions (multiplied by -1 in the negative region) is defined as the sea  
271 surface temperature index (DI\_SSTI). The ranges of positive and negative regions are (10°S–  
272 4°N, 170°E–160°W) and (0°–16°N, 129°E–155°E), respectively.

273 The second predictor is the leading 4-year autumn Bonin high (32°N–50°N, 130°E–165°E),  
274 which is an anticyclone over Japan (Fig. 3b). As a possible descending branch of the Hadley  
275 cell, the Bonin high (1) can induce a meridional overturning and PJ pattern is established  
276 (Enomoto et al. 2003; Hsu and Lin 2007; He et al. 2018). There is an anomalous strong  
277 westward flow on the south of the Bonin high, which makes humid in East Asia and the EASM  
278 increases accordingly (Wakabayashi and Kawamura 2004; Yasunaka and Hanawa 2006; Ming  
279 et al. 2019).

280 The third predictor is the leading 5-year Kara Sea SIC (77°N–80°N, 70°E–90°E) in summer  
281 (Fig. 4a). The changes of SIC are highly correlated with the variability of the EASM (Zhao et  
282 al. 2004; Wu et al. 2009a, b; Guo et al. 2013; Li et al. 2018; Lin and Li 2018). The SIC anomaly  
283 is closely related to changes in the extent of Eurasia snow cover (Fig. 4b) (Cohen et al. 2012;  
284 Li et al. 2018), which has an impact on EASM (Wu et al. 2009c) through affecting the soil  
285 moisture (Zhang and Zuo 2011). The reduction in SIC over the Kara Sea also may trigger an  
286 anomalous high in summer (Fig. 4c) through the European land surface acting as a “bridge”.  
287 The EASM is prevented from moving northward by the anomalous high and weakens (Zhao et  
288 al. 2004).

289 Fig. 5 shows time series of DI for each predictor and DI\_EASMI. The correlation  
290 coefficients of DI\_EASMI with DI\_SIC, DI\_SSTI and DI\_BH are 0.67, 0.47 and 0.59,  
291 respectively, all of which are significant at the 99% confidence level by the student’s t-test.  
292 Due to the long study period, the correlation between each predictor and DI\_EASMI may  
293 present decadal changes. The correlation between the Bonin high and the EASMI changed

294 abruptly at the end of the 1950s, and a weak correlation remained until the end of the 1970s  
295 (Fig. 6a). In addition to the weak correlation between DI\_SSTI and DI\_SIC occurred around  
296 1980, the correlation remained stable in other years (Fig. 6b, c). Therefore, on the whole, the  
297 three predictors are stably and significantly correlated with DI\_EASMI across the study period.

#### 298 **4. Prediction effect**

299 To evaluate the performance of the established statistical model, cross validation and  
300 independent hindcast are conducted in the present study. Results of the cross validation are  
301 displayed in Fig. 7a, which shows that the correlation coefficient between the predicted  
302 DI\_EASMI and the observation for the period 1921–2010 is 0.81, which is significant at the  
303 99% confidence level by the student's t-test. MSSS is 0.65. The predicted DI\_EASMI well  
304 captures the variability shown in observations during the study period except for the mid-1950s  
305 and the 1970s, when decadal variability of the related relationships occurred. This result  
306 indicates that the empirical statistical model developed in the present study has a high  
307 predictive skill. The DI\_EASMI predicted by the empirical statistical model is added to the  
308 leading 3-year observed EASMI to obtain predicted decadal EASMI. Except for the  
309 inconsistency that existed in the mid-1950s and the 1970s, the predicted EASMI realistically  
310 reproduces the positive phase over the period from the 1920s to the 1930s, the negative phase  
311 from around the late 1930s to the 1940s, the positive phase since the 1960s, the weaker EASM  
312 in the 1980s, and the intensification of the EASM in the early 1990s. The amplitude of the  
313 EASM oscillation is also quite consistent with observations. Furthermore, the correlation  
314 coefficient between the observed and predicted EASMI is 0.90 and MSSS is 0.78 (Fig. 7b and  
315 Table 1). In addition, the predicted EASMI well captures the regime shifts of the EASM due  
316 to its intensification in the 1940s and its weakening in the 1960s and 1970s as well as its  
317 intensification in the early 1990s. The prediction errors for these regime shifts all are less than

318 three years (Fig. 7c). The above results show that the decadal increment method has a high  
319 hindcast skill.

320 The hindcast skill is further verified based on the independent hindcast of the DI\_EASMI  
321 from 1980 to 2010. Fig. 7d shows that the variability displayed in observations is accurately  
322 grasped, and the correlation coefficient between the observed and the predicted DI\_EASMI is  
323 0.91, which is above the 99% confidence level by the student's t-test. MSSS is 0.81. The  
324 variability and amplitude of the predicted EASMI are quite consistent with observations,  
325 including the transition from negative to positive EASMI in the early 1990s. The correlation  
326 coefficient between the observations and predictions of the EASMI is 0.87, and MSSS is 0.72  
327 (Fig. 7e and Table 1). In addition, the predicted EASMI accurately captures the regime shift of  
328 the EASM in the early 1990s (Fig. 7f). Therefore, results of cross validation and independent  
329 hindcast indicate that the empirical statistical model combined with the decadal incremental  
330 method has a high skill of prediction for decadal variability of the EASM. The decadal regime  
331 shifts of the EASM can also be well captured.

## 332 **5. The real-time prediction for EASM in 2021**

333 Through the above analysis, it is found that the decadal increment method can effectively  
334 predict the long-term EASM. In this section, we operate a real-time prediction for EASMI in  
335 2021. The statistical forecast model is rebuilt for two main reasons. One is that there is few  
336 dataset covering the period from current to hundred years ago. The 20CR datasets used in above  
337 section ends at 2015. Therefore, we change to use the ERA5 dataset to operate the real-time  
338 prediction in this section. The other reason is that the relationship of the DI\_EASMI with  
339 DI\_SIC (DI\_BH) has weakened after 2010 (2004) (Fig. S1). The predictive skill of the Eq. 9  
340 for the DI\_EASMI becomes not reasonable during recent decade (Fig. S2). It is not surprised  
341 that the relationships between prediction and predictors have decadal shifts under the

342 background of many decadal shifts occurred in the climate (Krishnamurthy and Krishnamurthy  
343 2016; Notz 2017; Huang et al. 2018; Xu et al. 2019; Cai et al. 2021).

$$344 \quad DI\_EASMI = -0.85 * DI\_SIC - 0.37 * DI\_SST \quad (10)$$

345 The leading 4-year summer East Siberian Sea sea ice cover (71°–76°N, 150°–178°E) (Fig.  
346 8a) and leading 4-year summer South Indian Ocean (SIO) sea surface temperature (35°–44°S,  
347 70°–110°E) by removing the effect of East Siberian Sea sea ice cover (Fig. 9) are selected as  
348 predictors, which explain 72% and 14% of the DI\_EASMI variance, respectively. This  
349 indicates that the selected predictors can roughly reflect the characteristics of the EASM. The  
350 correlation coefficients of DI\_EASMI with DI\_SIC and DI\_SST are 0.85 and 0.37,  
351 respectively, both of which are significant at the 95% confidence level by the student's t-test.  
352 Their relationships have remained steady during most of the study period (Fig. 10), so they are  
353 selected as predictors.

354 Physically, the Arctic SIC is contributed to the EASM as previously discussed. As shown  
355 in Fig. 8b, the anomaly of sea ice in the East Siberian Sea possibly impacts SST anomalous in  
356 the North Pacific by affecting atmospheric circulation, which can persist into summer and  
357 influence the EASM circulation and precipitation (Guo et al. 2014). In addition, the SIO SST  
358 anomaly has an important impact on the interdecadal changes of the EASM at the end of the  
359 20th century (Xue 2001; Zhang et al. 2017). The decadal cooling in the SIO may lead to  
360 anomalous mid-tropospheric descents over the western SIO and anomalous ascents over the  
361 eastern SIO and the tropical Indian Ocean. The upper-level divergent flows converge over  
362 tropical East Asia, an anomalous low-level anticyclone is observed over the South China Sea-  
363 Philippines, thereby enhancing the EASM (Zhang et al. 2017).

364 In the cross validation, the correlation coefficient between the predicted DI\_EASMI and  
365 the observation for the period 1990–2018 is 0.90 and MSSS is 0.81 (Fig. 11a). The predicted

366 DI\_EASMI is added to the leading 3-year observed EASMI to obtain predicted EASMI. The  
367 correlation coefficient between the observed and predicted EASMI is 0.90 and MSSS is 0.78  
368 (Fig. 11b). In addition, the predicted EASMI well captures the regime shift of the EASM in the  
369 early 2000s (Fig. 11c). In the independent hindcast, the correlation coefficient between the  
370 observed and the predicted DI\_EASMI is 0.90 during 2011–2018, and MSSS is 0.79 (Fig. 11d).  
371 The correlation skill of the final predicted EASMI is 0.94, along with an MSSS of 0.87 (Fig.  
372 11e).

373       Regardless of cross validation or independent hindcast, the prediction model shows almost  
374 consistent results with observations, which increases our confidence in predicting future  
375 changes of EASM. According to the results of independent hindcast, EASM is relatively weak  
376 in 2019 and 2020, but it is likely to be a weak positive phase in 2021 (Fig. 11e). To explore  
377 whether 2021 will be a decadal regime shift, EASM in 2022 is further calculated. Different  
378 from the previous method, we consider using the predicted DI\_EASMI from the statistical  
379 model added to the prediction of EASMI three years ago from decadal increment method to  
380 get the re-predicted EASMI in 2022. This method was tested and the results show that the  
381 correlation coefficient between the re-predicted EASMI and the observation is 0.78 and MSSS  
382 is 0.51, and the variability of the predicted value is relatively consistent with observations (Fig.  
383 12). Therefore, EASM in 2022 is predicted by this method and it may return to a negative phase  
384 (Fig. 11e and Fig. 12), which means the chance of a decadal regime shift is relatively rare.

## 385 **6. Discussion**

386       To compare with the decadal increments method, the empirical statistical model in the  
387 original form is established, and the predictors are selected over the same areas as that selected  
388 for the decadal increment model (Eq. 9).

$$389 \quad \quad \quad EASMI = 0.41 * SSTI + 0.39 * BH + 0.48 * SIC \quad (11)$$

390 The correlation coefficients of decadal EASMI during the period 1921–2010 with the SIC, BH  
391 and sea surface temperature index (SSTI) are 0.51, 0.37, and 0.66, respectively. Results of the  
392 cross validation show that the correlation coefficient between observations and predictions of  
393 the EASMI by the empirical statistical model in the original form is 0.67 and MSSS is 0.43  
394 (Fig. 13a and Table 1), both of which are lower than that between observations and forecast of  
395 the empirical statistical model for decadal increment prediction (correlation coefficient and  
396 MSSS are 0.90 and 0.78 respectively). The empirical statistical model in the original form fails  
397 to capture the EASM variability, although it reproduces the negative phase around 1940, the  
398 positive phase in the early 1960s, the negative phase in the 1980s and the positive phase in the  
399 early 1990s (Fig. 13a). The model also cannot effectively capture the decadal regime shifts of  
400 the EASM (Fig. 13b). In the independent hindcast, the correlation coefficient between the  
401 predicted and the observed EASM from 1980 to 2010 is 0.76 (Fig. 13c and Table 1) and the  
402 decadal regime shift in the early 1990s is accurately grasped (Fig. 13d). However, the negative  
403 phase that began in the mid-1990s was mistakenly predicted as a positive phase, and MSSS is  
404 -1.39 (Table 1). This result indicates that the hindcast skill of the statistical model is quite  
405 limited. Therefore, using the decadal increment method to build a statistical model is helpful  
406 to improve the skill for the EASM prediction.

## 407 **7. Summary**

408 Based on previous research of decadal changes in the EASM and analysis of the  
409 relationship between the DI of predictors and DI\_EASMI, the present study develops the  
410 empirical statistical prediction model that is combined with the decadal increment method to  
411 predict decadal variability of the EASM.

412 The statistical model is valuable when the relationships between the predictant and the  
413 predictors remain stable during the study period. The process of model building is illustrated

414 in Fig. 14. First, based on the 5-year running mean EASMI, the 3-year decadal DI\_EASMI is  
415 calculated, that is, the running mean EASMI of the current year minus the EASMI three years  
416 ago. The leading 3-year summer DI\_SSTI over the equatorial Pacific, the leading 4-year  
417 DI\_BH in autumn and the leading 5-year summer DI\_SIC over the Kara Sea are then selected  
418 as predictors. Note that these predictors remain independent of each other. Compared with the  
419 method of selecting the original variables directly, the incremental method increases effective  
420 samples in the correlation analysis and obtains more useful decadal signals in the climate  
421 system from previous observations. Finally, the selected predictors are used to build the  
422 statistical model, and the final predicted EASMI is the predicted DI\_EASMI plus the observed  
423 EASMI three years ago. Results of cross validation from 1921 to 2010 indicate that the  
424 variability and amplitude of the predicted EASMI are quite consistent with the observed  
425 EASMI. Their correlation coefficient is 0.90, and MSSS is 0.78. The independent hindcast  
426 during the period 1980 to 2010 also shows that the variability and amplitude of the predicted  
427 EASMI are consistent with the observed EASMI. Their correlation coefficient is 0.87, and  
428 MSSS is 0.72. In addition, the predicted EASMI accurately captures the decadal regime shifts.  
429 The above results indicate that the decadal incremental method can well reproduce the  
430 characteristics of decadal variability of the EASM. Compared with the statistical model in the  
431 original form, the prediction skills of the model developed in this study are also improved,  
432 which makes it a great tool for future prediction of decadal changes in the EASM.

433 Therefore, this method is further used to build a real-time prediction model to predict the  
434 EASM in 2021 and 2022, the leading 4-year summer DI of the South Indian Ocean (SIO) sea  
435 surface temperature and the leading 4-year summer DI of the East Siberian Sea sea ice cover  
436 are selected as predictors. The results show that EASM is in a negative phase in 2019 and  
437 2020, but it may be in a weak positive phase in 2021 and will go back to a negative phase in  
438 2022.

439 Using the decadal increment method, preliminary attempts have been made to predict  
440 decadal variability in the EASM, and satisfactory results have been achieved. This study  
441 provides a new solution for the prediction of decadal variability. In the future, machine learning  
442 combined with this method can replace multiple linear regression for the prediction of other  
443 climate phenomena, such as decadal variability of drought in North China. Since the predictive  
444 effect of the decadal increment method is better than that of the original form, it can also be  
445 applied for decadal prediction in climate dynamic models, which may further improve the  
446 predictive skill of climate models.  
447

448

## REFERENCES

- 449 Bretherton CS, Widmann M, Dymnikov VP, Wallace JM, Bladé I (1999) The effective number  
450 of spatial degrees of freedom of a time-varying field. *J Clim* 12(7):1990–2009.  
451 [https://doi.org/10.1175/1520-0442\(1999\)012<1990:TENOSD>2.0.CO;2](https://doi.org/10.1175/1520-0442(1999)012<1990:TENOSD>2.0.CO;2).
- 452 Cai QQ, Beletsky D, Wang J, Lei RB (2021) Interannual and decadal variability of Arctic  
453 summer sea ice associated with atmospheric teleconnection patterns during 1850-2017. *J*  
454 *Clim* 1-89. <https://doi.org/10.1175/JCLI-D-20-0330.1>.
- 455 Chen LX, Zhu CW, Wang W, Zhang PQ (2001) Analysis of the Characteristics of 30–60 Day  
456 Low-Frequency Oscillation over Asia during 1998 SCSMEX. *Adv Atmos Sci* 18:623-638.  
457 <https://doi.org/10.1007/s00376-001-0050-0>.
- 458 Cohen JL, Furtado CJ, Barlow MA, Alexeev VA, Cherry JE (2012) Arctic warming, increasing  
459 snow cover and widespread boreal winter cooling. *Environ Res Lett*, 7:014007.  
460 <https://doi.org/10.1088/1748-9326/7/1/014007>.
- 461 Compo GP, et al (2011) The Twentieth Century Reanalysis Project. *Quart J Roy Meteor Soc*  
462 137(654):1–28. <https://doi.org/10.1002/qj.776>.
- 463 Ding YH (1994) *Monsoon over China*. Netherlands: Kluwer Academic Publishers, 420.
- 464 Ding YH, Wang ZY, Sun Y (2008) Inter-decadal variation of the summer precipitation in East  
465 China and its association with decreasing Asian summer monsoon. Part I: observed  
466 evidences. *Int J Climatol* 28:1139–1161. <https://doi.org/10.1002/joc.1615>.
- 467 Ding YH, Sun Y, Wang ZY, Zhu YX, Song YF (2009) Inter-decadal variation of the summer  
468 precipitation in China and its association with decreasing Asian summer monsoon Part II:  
469 Possible causes. *Int J Climatol* 29(13):1926-1944. <https://doi.org/10.1002/joc.1759>.

470 Ding YH et al (2013) Interdecadal and interannual variabilities of the Asian summer monsoon  
471 and its projection of future change. *Chin J Atmos Sci* 37 (2):253–280.  
472 <https://doi.org/10.3878/j.issn.1006-9895.2012.12302>. (in Chinese)

473 Ding YH et al (2018) On the characteristics, driving forces and inter-decadal variability of the  
474 East Asian summer monsoon. *Chin J Atmos Sci* 42 (3):533-558.  
475 <https://doi.org/10.3878/j.issn.1006-9895.1712.17261>. (in Chinese)

476 Doblas-Reyes FJ et al (2013) Initialized near-term regional climate change prediction. *Nat*  
477 *Commun* 4:1715. <https://doi.org/10.1038/ncomms2704>.

478 Dong X, Xue F (2016) Phase transition of the Pacific decadal oscillation and decadal variation  
479 of the East Asian summer monsoon in the 20th century. *Adv Atmos Sci* 33(3):330–338.  
480 <https://doi.org/10.1007/s00376-015-5130-7>.

481 Enomoto T, Hoskins BJ, Matsuda Y (2003) The formation mechanism of the Bonin high in  
482 August. *Quart J Roy Meteor Soc* 157-178. <https://doi.org/10.1256/qj.01.211>.

483 Fan K, Wang HJ, Choi YJ (2008) A physically-based statistical forecast model for the middle-  
484 lower reaches of the Yangtze River Valley summer rainfall. *Chin Sci Bull* 53(4):602-609.  
485 <https://doi.org/10.1007/s11434-008-0083-1>.

486 Goddard L et al (2012) A verification framework for interannual-to-decadal predictions  
487 experiments. *Clim Dyn* 40:245–272. <https://doi.org/10.1007/s00382-012-1481-2>.

488 Gong DY, Ho CH (2002) Shift in the summer rainfall over the Yangtze River valley in the late  
489 1970s. *Geophys Res Lett* 29(10):78-71-78-74. <https://doi.org/10.1029/2001GL014523>.

490 Guan B, Chan JCJ (2006) Nonstationary of the intraseasonal oscillations associated with the  
491 Western North Pacific summer monsoon. *J Clim* 19:622–629.  
492 <https://doi.org/10.1175/JCLI3661.1>.

493 Guo D et al (2013) Mechanism on how the spring Arctic sea ice impacts the East Asian summer  
494 monsoon. *Theor Appl Climatol* 115(1-2):107-119.  
495 <https://doi.org/10.1007/s00704-013-0872-6>.

496 Guo QY, Cai JN, Shao XM, Sha WY (2003) Interdecadal variability of East Asian summer  
497 monsoon and its impact on the climate of China. *Acta Geol Sin* 58:569–576.  
498 <https://doi.org/10.3321/j.issn:0375-5444.2003.04.011>. (in Chinese)

499 Ha KJ, Heo KY, Lee SS, Yun KS, Jhun JJ (2012) Variability in the East Asian monsoon: a  
500 review. *Meteorol Appl* 19:200–215. <https://doi.org/10.1002/met.1320>.

501 He C, Zhou TJ, Wu B (2015) The Key Oceanic Regions Responsible for the Interannual  
502 Variability of the Western North Pacific Subtropical High and Associated Mechanisms. *J*  
503 *Meteor Res* 29(4):562-575. <https://doi.org/10.1007/s13351-015-5037-3>.

504 Hersbach H et al (2020) The ERA5 global reanalysis. *Quart J Roy Meteor Soc* 146:1999–2049.  
505 <https://doi.org/10.1002/qj.3803>.

506 Hsu HH, Liu X (2003) Relationship between the Tibetan Plateau heating and East Asian  
507 summer monsoon rainfall. *Geophys Res Lett* 30:2066.  
508 <https://doi.org/10.1029/2003GL017909>.

509 Hu Z (1997) Interdecadal variability of summer climate over East Asia and its association with  
510 500 hPa height and global sea surface temperature. *J Geophys Res Atmos*  
511 102(D16):19403–19412. <https://doi.org/10.1029/97JD01052>.

512 Huang RH, Chen W, Yang BL, Zhang RH (2004) Recent advances in studies of the interaction  
513 between the East Asian winter and summer monsoons and ENSO cycle. *Adv Atmos Sci*  
514 21(3):407-424. <https://doi.org/10.1007/BF02915568>.

515 Huang RH, Huang G, We ZG (2004) Climate variations of the summer Asian monsoon over  
516 China. In: Chang CP (ed) *East Asian Monsoon*. World Scientific, pp 564.

517 Huang RH, Chen JL, Huang G (2007) Characteristics and variations of the East Asian monsoon  
518 system and its impacts on climate disasters in China. *Adv Atmos Sci* 24(6):993-1023.  
519 <https://doi.org/10.1007/s00376-007-0993-x>.

520 Huang RH, Chen JL, Liu Y (2011) Interdecadal variation of the leading modes of summertime  
521 precipitation anomalies over eastern China and its association with water vapor transport  
522 over East Asia. *Chin J Atmos Sci* 35 (4):589–606. [https://doi.org/10.3878/j.issn.1006-](https://doi.org/10.3878/j.issn.1006-9895.2011.04.01)  
523 [9895.2011.04.01](https://doi.org/10.3878/j.issn.1006-9895.2011.04.01). (in Chinese)

524 Huang YY, Li XF (2015) The interdecadal Variation of the western Pacific subtropical high as  
525 measured by 500hPa eddy geopotential height. *Atmos Ocean Sci Lett* 8:371-375.  
526 <https://doi.org/10.3878/AOSL20150038>.

527 Huang YY, Wang HJ, Fan K, Gao YQ (2015) The western pacific subtropical high after the  
528 1970s: westward or eastward shift? *Clim Dyn* 44(7-8):2035-2047.  
529 <https://doi.org/10.1007/s00382-014-2194-5>.

530 Huang YY, Wang B, Li XF, Wang HJ (2018) Changes in the influence of the western Pacific  
531 subtropical high on Asian summer monsoon rainfall in the late 1990s. *Clim Dyn* 51:443-  
532 455. <https://doi.org/10.1007/s00382-017-3933-1>.

533 Huang YY, Wang HJ (2020a) A Possible Approach for Decadal Prediction of the PDO. *J*  
534 *Meteor Res* 34(1):63-72. <https://doi.org/10.1007/s13351-020-9144-4>.

535 Huang YY, Wang HJ (2020b) Is the Regional Precipitation Predictable in Decadal Scale? A  
536 Possible Approach for the Decadal Prediction of the Summer Precipitation Over North  
537 China. *Earth Space Sci* 7(1). <https://doi.org/10.1029/2019EA000986>.

538 Kim HM, Webster PJ, Curry JA (2012) Evaluation of short-term climate change prediction in  
539 multi-model CMIP5 decadal hindcasts. *Geophys Res Lett* 39:L10701.  
540 <https://doi.org/10.1029/2012GL051644>.

- 541 Kirtman B et al (2013) Near-term climate change: Projections and predictability. In *Climate*  
542 *change 2013: The physical science basis: Working Group I Contribution to the Fifth*  
543 *Assessment Report of the Intergovernmental Panel on Climate Change*. Cambridge  
544 University Press, 953-1028.
- 545 Krishnamurthy L, Krishnamurthy V (2016) Decadal and interannual variability of the Indian  
546 Ocean SST. *Clim Dyn* 46(1–2):57–70. <https://doi.org/10.1007/s00382-015-2568-3>.
- 547 Li HM, Dai AG, Zhou TJ, Lu J (2008) Responses of East Asian summer monsoon to historical  
548 SST and atmospheric forcing during 1950–2000. *Clim Dyn* 34(4):501-514.  
549 <https://doi.org/10.1007/s00382-008-0482-7>.
- 550 Li HX, Chen HP, Wang HJ, Sun JQ, Ma JH (2018) Can Barents sea ice decline in spring  
551 enhance summer hot drought events over north-eastern China? *J. Clim* 31(12):4705–4725.  
552 <https://doi.org/10.1175/JCLI17-0429.1>.
- 553 Liu HW, Zhou TJ, Zhu YX, Lin YH (2012) The strengthening East Asia summer monsoon  
554 since the early 1990s. *Chin Sci Bull* 57(13):1553-1558. [https://doi.org/10.1007/s11434012-](https://doi.org/10.1007/s11434012-4991-8)  
555 [4991-8](https://doi.org/10.1007/s11434012-4991-8).
- 556 Lin Z, Li F (2018) Impact of interannual variations of spring sea ice in the Barents Sea on east  
557 Asian rainfall in June. *Atmos Ocean Sci Lett* 11:275–281.  
558 <https://doi.org/10.1080/16742834.2018.1454249>.
- 559 Lü JM, Zhu CW, Ju JH, Lin X (2014) Interdecadal variability in summer precipitation over  
560 East China during the past 100 years and its possible causes. *Chin J Atmos Sci* 38  
561 (4):782–794. <https://doi.org/10.3878/j.issn.1006-9895.1401.13227>. (in Chinese)
- 562 Mao JY, Chan JC (2005) Intraseasonal variability of the South China Sea summer monsoon.  
563 *J. Clim* 18:2388–2402. <https://doi.org/10.1175/JCLI3395.1>.

564 Meehl GA, Arblaster JM (2002) The tropospheric biennial oscillation and Asian-Australian  
565 monsoon rainfall. *J Clim* 15:722–744. [https://doi.org/10.1175/1520-  
566 0442\(2002\)015<0722:TTBOAA>2.0.CO;2](https://doi.org/10.1175/1520-0442(2002)015<0722:TTBOAA>2.0.CO;2).

567 Meehl GA et al (2014) Decadal climate prediction: An update from the trenches. *Bull Amer  
568 Meteor Soc* 95(2):243–267. <https://doi.org/10.1175/BAMS-D-12-00241.1>.

569 Ming J, Sun JQ, Yu S (2019) Combined impact of the pacific–japan pattern and mediterranean–  
570 northern eurasia pattern on east asian summer temperatures. *Atmos Ocean Sci Lett* 12(3):  
571 1-10. <https://doi.org/10.1080/16742834.2019.1585101>.

572 Murphy AH (1988) Skill scores based on the mean square error and their relationships to the  
573 correlation coefficient. *Mon Weather Rev* 116(12):2417–2424.  
574 [https://doi.org/10.1175/1520-0493\(1988\)116<2417:SSBOTM>2.0.CO;2](https://doi.org/10.1175/1520-0493(1988)116<2417:SSBOTM>2.0.CO;2).

575 Notz D (2017) Arctic sea ice seasonal-to-decadal variability and long- term change. *Past Glob  
576 Changes Mag* 72:14–9. <https://doi.org/10.22498/pages.25.1.14>.

577 Rayner NA et al (2003) Global analyses of sea surface temperature, sea ice, and night marine  
578 air temperature since the late nineteenth century. *J Geophys Res Atmos* 108(D14):4407.  
579 <https://doi.org/10.1029/2002JD002670>.

580 Si D, Ding YH, Liu YJ (2009) Decadal northward shift of the Meiyu belt and the possible  
581 cause. *Chin Sci Bull* 54(24):4742–4748. <https://doi.org/10.1007/s11434-009-0385-y>.

582 Smith TM, Reynolds RW, Peterson TC, Lawrimore JH (2008) Improvements to NOAA's  
583 historical merged land-ocean surface temperature analysis (1880-2006). *J. Clim*  
584 21(10):2283–2296. <https://doi.org/10.1175/2007JCLI2100.1>.

585 Tao SY, Chen LX (1987) A review of recent research on the East Asian summer monsoon in  
586 China. In: Chang CP, Krishnamurti TN (ed) *Monsoon Meteorology*. Oxford University  
587 Press, pp 60–92.

- 588 Tong Q, Huang YY, Duan MK, Zhao QF (2020) Possible contribution of the pdo to the  
589 eastward retreat of the western pacific subtropical high. *Atmos Ocean Sci Lett* 100005.  
590 <https://doi.org/10.1016/j.aosl.2020.100005>.
- 591 Vihma T (2014) Effects of Arctic Sea Ice Decline on Weather and Climate: A Review. *Surv.*  
592 *Geophys* 35(5):1175-1214. <https://doi.org/10.1007/s10712-014-9284-0>.
- 593 Wakabayashi S, Kawamura R (2004) Extraction of Major Teleconnection Patterns Possibly  
594 Associated with the Anomalous Summer Climate in Japan. *J Meteorol Soc Japan*  
595 82(6):1577-1588. <https://doi.org/10.2151/jmsj.82.1577>.
- 596 Wang B, Wu RG, Fu XH (2000) Pacific-East Asian teleconnection: how does ENSO affect  
597 East Asian climate? *J Clim* 13:1517–1536. [https://doi.org/10.1175/1520-0442\(2000\)013<1517:PEATHD>2.0.CO;2](https://doi.org/10.1175/1520-0442(2000)013<1517:PEATHD>2.0.CO;2).
- 599 Wang B, Xiang BQ, Lee JY (2013) Subtropical High predictability establishes a promising  
600 way for monsoon and tropical storm predictions. *P Natl A Sci* 110:2718–2722.  
601 <https://doi.org/10.1073/pnas.1214626110>.
- 602 Wang B et al (2018) Toward Predicting Changes in the Land Monsoon Rainfall a Decade in  
603 Advance. *J. Clim* 31:2699-2714. <https://doi.org/10.1175/JCLI-D-17-0521.1>.
- 604 Wang HJ, Zhou GQ, Zhao Y (2000) An effective method for correcting the seasonal-  
605 interannual prediction of summer climate anomaly. *Adv Atmos Sci* 17(2):234-240.  
606 <https://doi.org/10.1007/s00376-000-0006-9>.
- 607 Wang HJ (2001) The weakening of the Asian monsoon circulation after the end of 1970's. *Adv*  
608 *Atmos Sci* 18:376–386. <https://doi.org/10.1007/BF02919316>.
- 609 Wang HJ (2002) The instability of the East Asian summer Monsoon-ENSO relations. *Adv*  
610 *Atmos Sci* 19:1-11. <https://doi.org/10.1007/s00376-002-0029-5>.

- 611 Wang HJ et al (2012) Initiating and applying the interannual increment prediction approach  
612 Advances in Climate Prediction Theory and Technique of China. China Meteorological  
613 Press, pp 120–139. (in Chinese).
- 614 Wu BY, Zhang RH, Ding YH, D'Arrigo R (2008) Distinct modes of the East Asian summer  
615 monsoon. *J. Clim* 21:1122–1138. <https://doi.org/10.1175/2007JCLI1592.1>.
- 616 Wu BY, Zhang RH, Wang B, D'Arrigo R (2009a) On the association between spring Arctic  
617 sea ice concentration and Chinese summer rainfall. *Geophys Res Lett* 36(9).  
618 <https://doi.org/10.1029/2009GL037299>.
- 619 Wu BY, Zhang RH, Wang B (2009b) On the association between spring Arctic sea ice  
620 concentration and Chinese summer rainfall: A further study. *Adv Atmos Sci* 26(4):666–678.  
621 <https://doi.org/10.1007/s00376-009-9009-3>.
- 622 Wu BY, Yang K, Zhang RH (2009c) Eurasian snow cover variability and its association with  
623 summer rainfall in China. *Adv Atmos Sci* 26(1):31–44. [https://doi.org/10.1007/s00376-](https://doi.org/10.1007/s00376-009-0031-2)  
624 [009-0031-2](https://doi.org/10.1007/s00376-009-0031-2).
- 625 Wu B, Zhou TJ, Li C, Müller WA, Lin J (2019) Improved decadal prediction of Northern-  
626 Hemisphere summer land temperature. *Clim Dyn* 53:1357–1369.  
627 <https://doi.org/10.1007/s00382-019-04658-8>.
- 628 Wu GX, Chou JF, Liu YM, Zhang QY, Sun SQ (2003) Review and prospect of the study on  
629 the subtropical anticyclone. *Chin J Atmos Sci* 27:503e517.  
630 <https://doi.org/10.3878/j.issn.1006-9895.2003.04.06>. (in Chinese)
- 631 Xu M, et al (2006) Steady decline of East Asian monsoon winds, 1969–2000: evidence from  
632 direct ground measurements of wind speed. *J Geophys Res Atmos* 111:D24111.  
633 <https://doi.org/10.1029/2006JD007337>.

634 Xu XP, et al (2019) Strengthened linkage between midlatitudes and Arctic in boreal winter.  
635 Clim Dyn 53:3971–3983. <https://doi.org/10.1007/s00382-019-04764-7>.

636 Xue F (2001) Interannual to Interdecadal variation of East Asian summer monsoon and its  
637 association with the global atmospheric circulation and sea surface temperature. *Adv Atmos*  
638 *Sci* 18:567–575. <https://doi.org/10.1007/s00376-001-0045-x>.

639 Yasunaka S, Hanawa K (2006) Interannual Summer Temperature Variations over Japan and  
640 Their Relation to Large-Scale Atmospheric Circulation Field. *J Meteorol Soc Japan*  
641 84:641-652. <https://doi.org/10.2151/jmsj.84.641>.

642 Ye X, Zhang W, Luo M (2016) The North Pacific Gyre Oscillation and East Asian summer  
643 precipitation. *Atmos Sci Lett* 17:531–537. <https://doi.org/10.1002/asl.688>.

644 Ying M, Sun SQ (2000) A study on the response of subtropical high over the western Pacific  
645 on the SST anomaly. *Chin J Atmos Sci* 24:193–206.  
646 <https://doi.org/10.1007/s10011-000-0335-3>. (in Chinese)

647 Yu L (2013) Potential correlation between the decadal East Asian summer monsoon variability  
648 and the Pacific decadal oscillation. *Atmos Ocean Sci Lett* 6:394–397.  
649 <https://doi.org/10.3878/j.issn.1674-2834.13.0040>.

650 Yu RC, Wang B, Zhou TJ (2004) Tropospheric cooling and summer monsoon weakening trend  
651 over East Asia. *Geophys Res Lett* 31(22):L22212. <https://doi.org/10.1029/2004GL021270>.

652 Yu RC, Zhou TJ (2007) Seasonality and three-dimensional structure of interdecadal change in  
653 the East Asian monsoon. *J. Clim* 20(21):5344-5355.  
654 <https://doi.org/10.1175/2007JCLI1559.1>.

655 Zhang HY, Wen ZP, Wu RG, Chen ZS, Guo YY (2016) Inter-decadal changes in the East  
656 Asian summer monsoon and associations with sea surface temperature anomaly in the

657 South Indian Ocean. *Clim Dyn* 48(3-4):1125-1139.  
658 <https://doi.org/10.4172/2157-7617.C1.027>.

659 Zhang RH, Sumi A, Kimoto M (1999) A diagnostic study of the impact of El Niño on the  
660 precipitation in China. *Adv Atmos Sci* 16:229–241. <https://doi.org/10.1007/BF02973084>.

661 Zhang RH, Zuo Z (2011) Impact of spring soil moisture on surface energy balance and summer  
662 monsoon circulation over East Asia and precipitation in East China. *J. Clim* 24(13):3309–  
663 3322. <https://doi.org/10.1175/2011JCLI4084.1>.

664 Zhao P, Zhang XD, Zhou XJ, Ikeda M, Yin YH (2004) The Sea Ice Extent Anomaly in the  
665 North Pacific and Its Impact on the East Asian Summer Monsoon Rainfall. *J Clim*  
666 17(17):3434-3447. [https://doi.org/10.1175/1520-  
667 0442\(2004\)017<3434:TSIEAI>2.0.CO;2](https://doi.org/10.1175/1520-0442(2004)017<3434:TSIEAI>2.0.CO;2).

668 Zhou TJ et al (2009) Why the western pacific subtropical high has extended westward since  
669 the late 1970s. *J. Clim* 22(8):2199-2215. <https://doi.org/10.1175/2008JCLI2527.1>.

670 Zhou TJ, Wu B (2017) Decadal climate prediction: Scientific frontier and challenge. *Adv Earth*  
671 *Sci* 32:331–341. <https://doi.org/10.11867/j.issn.1001-8166.2017.04.0331>. (in Chinese)

672 Zhu YL, Wang HJ, Zhou W, Ma JH (2010) Recent changes in the summer precipitation pattern  
673 in East China and the background circulation. *Clim Dyn* 36(7–8):1463–1473.  
674 <https://doi.org/10.1007/s00382-010-0852-9>.

675 Zuo JQ, Li WJ, Sun CH, Xu L, Ren HL (2013) Impact of the North Atlantic sea surface  
676 temperature tripole on the East Asian summer monsoon. *Adv Atmos Sci* 30(4):1173–1186.  
677 <https://doi.org/10.1007/s00376-012-2125-5>.

678

679

TABLE

680 Table 1: The predictive skill of the statistical model combined with the increment method for the DI\_EASMI  
681 and EASMI.

682

## Figures

683

684 Fig. 1 **a** Decadal EASMI during 1918–2010 and **b** DI\_EASMI during 1921–2010

685

686 Fig. 2 Skewness coefficient (red bar) and kurtosis coefficient (blue bar) of decadal EASMI and DI\_EASMI.  
687 “0” represents decadal EASMI, “1”, “2”, and “3” represent 1-year, 2-year, and 3-year increment of decadal  
688 EASMI, respectively

689

690 Fig. 3 Correlation coefficients between DI\_EASMI during 1921–2010 and the leading DI of predictors (a 3-  
691 year leading sea surface temperature in summer (June to August); b 4-year leading Bonin high in Autumn  
692 (September to November). Dotted areas indicate values significant at the 95% confidence level by the  
693 student’s t-test, and the boxes indicate the key areas of the predictors, including DI\_SSTI (10°S–4°N, 170°E–  
694 160°W) and (0°–16°N, 129°E–155°E), DI\_BH (32°N–50°N, 130° E–165°E)

695

696 Fig. 4 **a** Correlation coefficient between DI\_EASMI during 1921–2010 and the leading 5-year DI of sea ice  
697 concentration in summer (June to August). The box indicates the key area of the predictor, and area-weighted  
698 regionally averaged DI\_SIC (77°S–80°N, 70°E–90°E) is used as a predictor. Correlation coefficient of the  
699 summer DI\_SIC during 1916–2005 with **b** the spring (March to May) DI of snow cover during 1921–2010  
700 and **c** the summer DI of 850hPa geopotential height during 1921–2010. Dotted areas indicate values  
701 significant at the 95% confidence level by the student’s t-test

702

703 Fig. 5 Time series of DI\_EASMI during 1921–2010 (black line) and 3-year leading DI\_SSTI (blue line), 4-  
704 year leading DI\_BH (green line) and 5-year leading DI\_SIC (red line)

705

706 Fig. 6 25-year running correlation between DI\_EASMI during 1921–2010 and leading DI of predictors (**a**  
707 BH, **b** SSTI, **c** SIC). The dotted line is at the 95% confidence level by the student’s t-test, and the effective  
708 sample numbers are 22, 23, and 22, respectively

709

710 Fig. 7 Predictions of **a, d** DI\_EASMI and **b, e** EASMI and **c, f** the results of the moving t-test with a 10-year  
711 moving window of EASMI (**a, b, c** results of the cross validation during 1921–2010; **d, e, f** results of  
712 independent hindcast during 1980–2010; the light pink shading indicates the 95% confidence interval of the  
713 prediction. The value in the upper right corner is the correlation coefficient/MSSS between observations and  
714 predictions; the thin solid lines in **c** and **f** are significant at the 95% confidence levels)

715

716 Fig. 8 **a** Correlation coefficient between DI\_EASMI during 1990–2018 and the leading 4-year summer (June  
717 to August) DI of sea ice cover. The box indicates the key area of the predictor, and area-weighted regionally  
718 averaged DI\_SIC (71°–76°N, 150°–178°E) is used as a predictor. **b** Correlation coefficient between summer  
719 DI\_SIC during 1986–2014 and the spring (March to May) DI of sea surface temperature during 1990–2018.  
720 Dotted areas indicate values significant at the 95% confidence level by the student’s t-test

721 Fig. 9 Correlation coefficient between DI\_EASMI during 1990–2018 and the 4-year leading DI of sea  
722 surface temperature in summer (June to August). Dotted areas indicate values significant at the 95%  
723 confidence level by the student's t-test, and the box indicates the key area of the predictor, including DI\_SST  
724 (35°S–44°S, 70°E–110°E)

725

726 Fig. 10 Time series of DI\_EASMI during 1990–2018 (black line) and 4-year leading DI\_SST (blues line)  
727 and DI\_SIC (red line) during 1990–2022

728

729 Fig. 11 Predictions of **a, d** DI\_EASMI and **b, e** EASMI and **c** the results of the moving t-test with a 9-year  
730 moving window of EASMI (**a, b, c** results of the cross validation during 1990–2018; **d, e** results of  
731 independent hindcast during 2011–2022; the light pink shading indicates the 95% confidence interval of the  
732 prediction. The value in the upper right corner is the correlation coefficient/MSSS between observations and  
733 predictions; the thin solid lines in **c** are significant at the 95% confidence levels by the student's t-test)

734

735 Fig. 12 Re-predictions of EASMI during 1993–2022, which is obtained by adding the predicted DI\_EASMI  
736 from statistical model to the EASMI prediction result three years ago from decadal increment (left of the  
737 dotted line: results of the cross validation during 1993–2013; right of the dotted line: results of the  
738 independent hindcast during 2014–2022). The light pink shading indicates the 95% confidence interval of  
739 the prediction. The value in the upper right corner is the correlation coefficient/MSSS between observations  
740 and predictions

741

742 Fig. 13 Direct predictions of EASMI **a, c** based on statistical prediction model in the original form and **b, d**  
743 the results of the moving t-test with a 10-year moving window (**a, c** results of the cross validation during  
744 1921–2010; **b, d** results of independent hindcast during 1980–2010; the light pink shading indicates the 95%  
745 confidence interval of the prediction. The value in the upper right corner is the correlation coefficient/MSSS  
746 between observations and predictions; the thin solid lines in **b** and **d** are significant at the 95% confidence  
747 levels by the student's t-test)

748

749 Fig. 14 Schematic diagram illustrating the process of predicting EASM using the decadal increment method

750

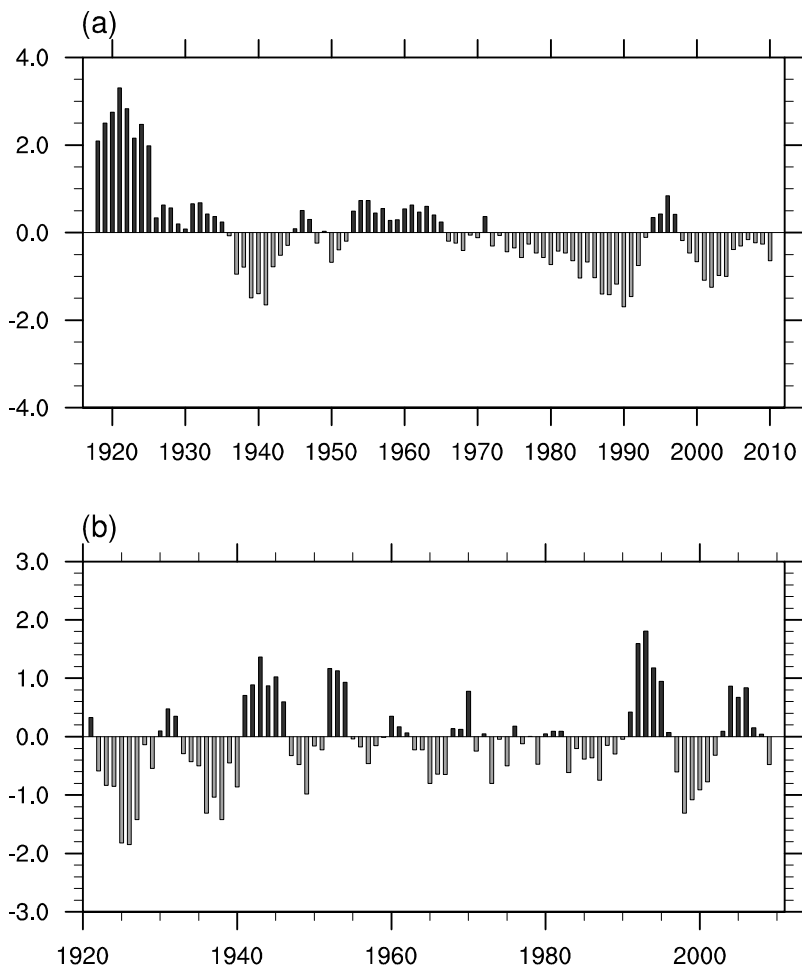
TABLE

	Cross validation (1921–2010)		Independent hindcast (1980–2010)	
	CC	MSSS	CC	MSSS
DI_EASMI	0.81	0.65	0.91	0.81
EASMI	0.90(0.65)	0.78(0.42)	0.87(0.76)	0.72(-1.39)

751

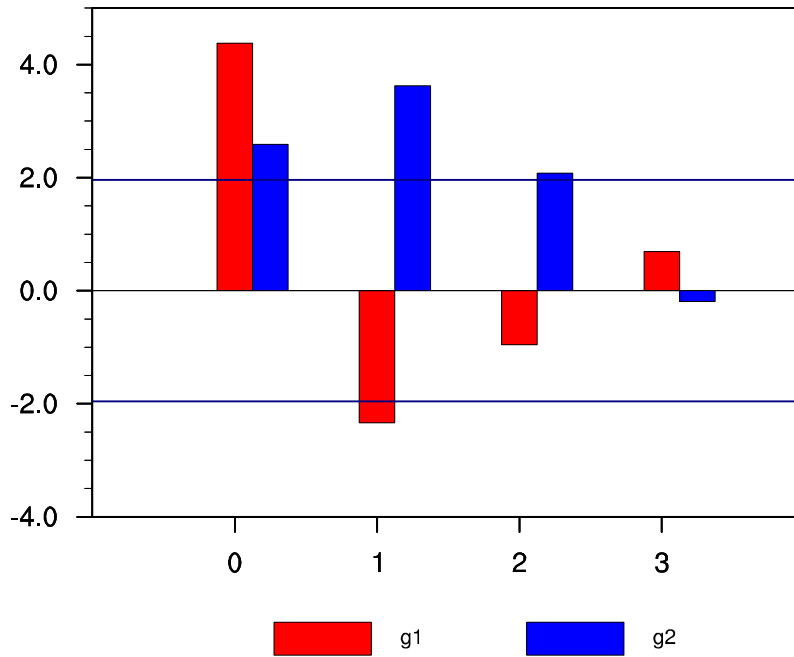
752 Table 1: The predictive skill of the statistical model combined with the increment method for the DI\_EASMI  
753 and EASMI.

754 Note: The results predicted by the statistical model in the original form are shown in parentheses. CC is the  
755 correlation coefficient and MSSS is the mean square skill score.



757

758 Fig. 1 **a** Decadal EASMI during 1918–2010 and **b** DI\_EASMI during 1921–2010

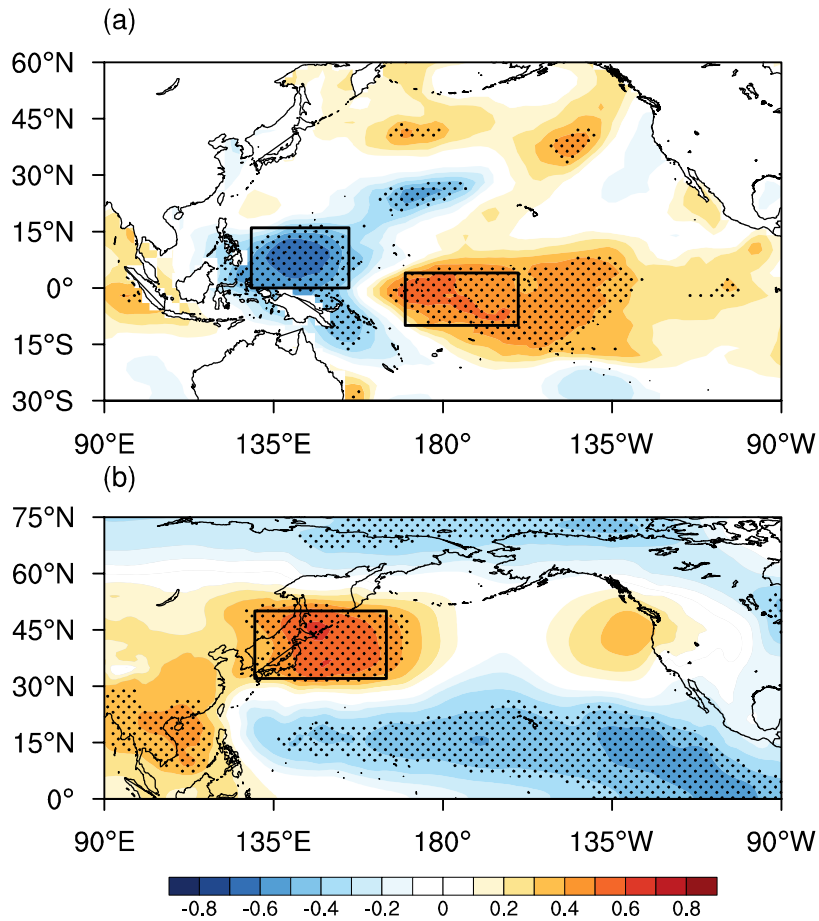


759

760 Fig. 2 Skewness coefficient (red bar) and kurtosis coefficient (blue bar) of decadal EASMI and DI\_EASMI.

761 "0" represents decadal EASMI, "1", "2", and "3" represent 1-year, 2-year, and 3-year increment of decadal

762 EASMI, respectively



763

764

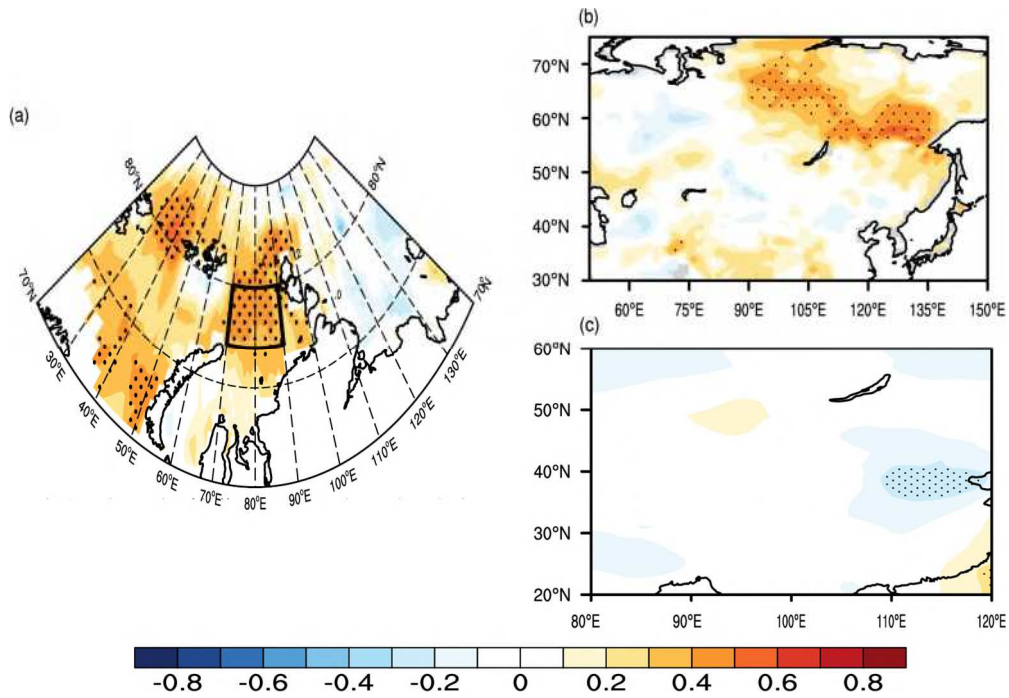
765

766

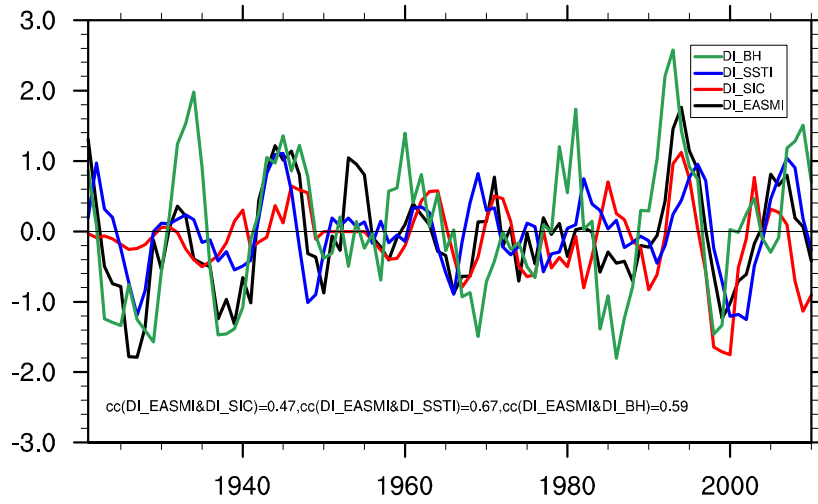
767

768

Fig. 3 Correlation coefficients between DI\_EASMI during 1921–2010 and the leading DI of predictors (a 3-year leading sea surface temperature in summer (June to August); b 4-year leading Bonin high in Autumn (September to November)). Dotted areas indicate values significant at the 95% confidence level by the student's t-test, and the boxes indicate the key areas of the predictors, including DI\_SSTI (10°S–4°N, 170°E–160°W) and (0°–16°N, 129°E–155°E), DI\_BH (32°N–50°N, 130° E–165°E)



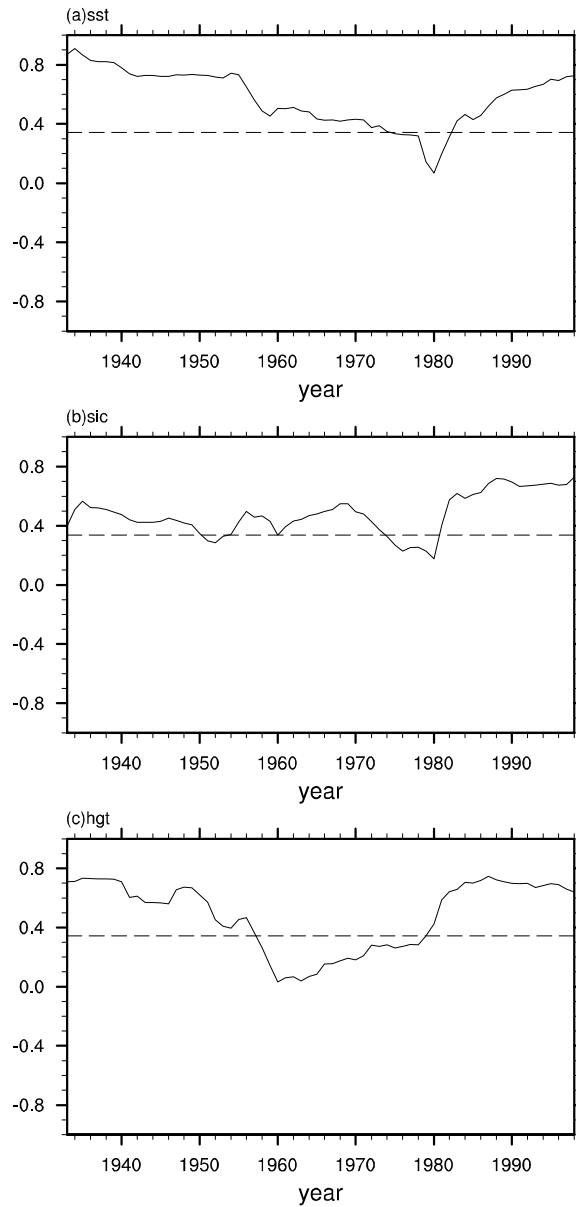
769  
 770 Fig. 4 **a** Correlation coefficient between DI\_EASMI during 1921–2010 and the leading 5-year DI of sea ice  
 771 concentration in summer (June to August). The box indicates the key area of the predictor, and area-weighted  
 772 regionally averaged DI\_SIC (77°S–80°N, 70°E–90°E) is used as a predictor. Correlation coefficient of the  
 773 summer DI\_SIC during 1916–2005 with **b** the spring (March to May) DI of snow cover during 1921–2010  
 774 and **c** the summer DI of 850hPa geopotential height during 1921–2010. Dotted areas indicate values  
 775 significant at the 95% confidence level by the student’s t-test



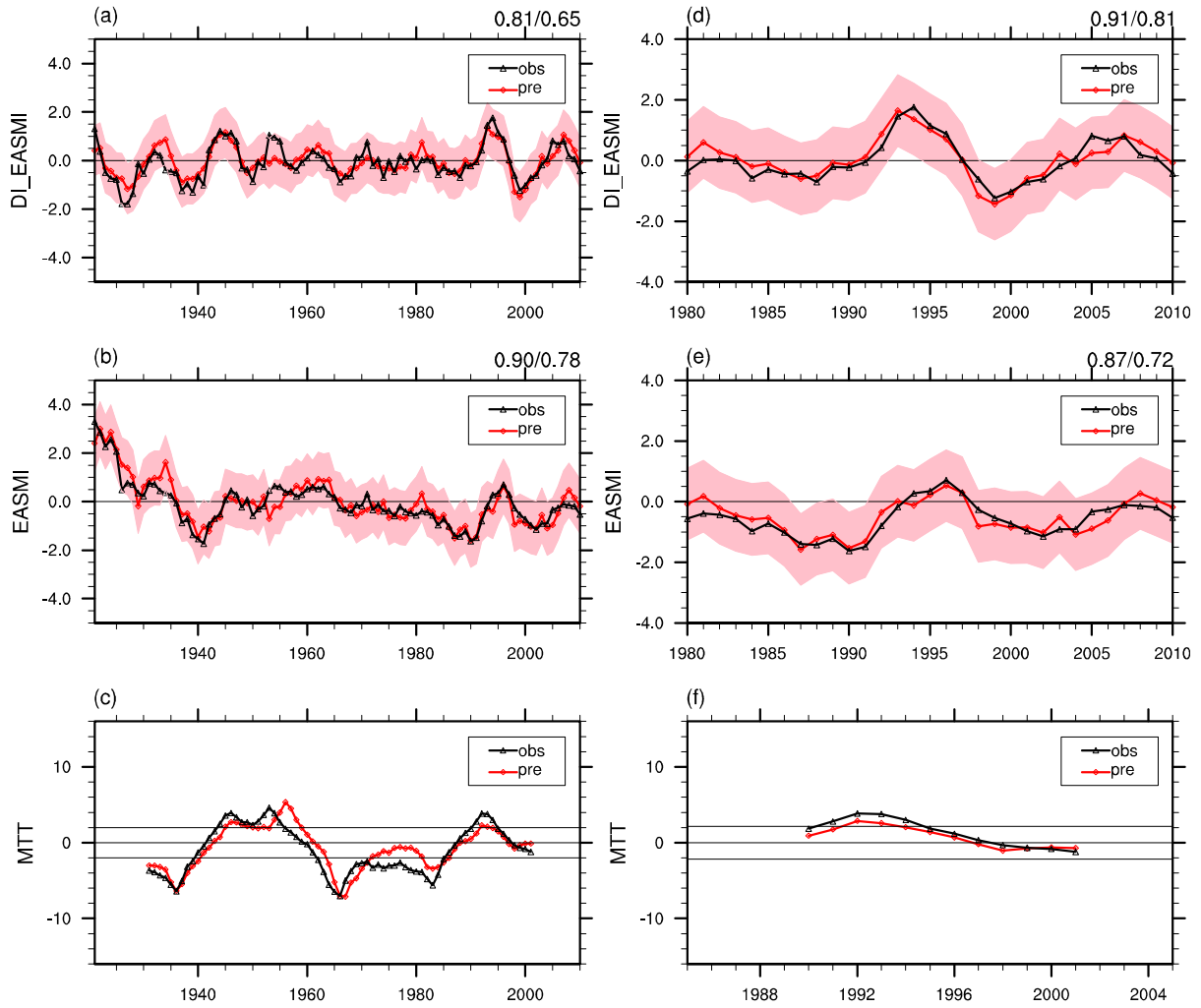
776

777 Fig. 5 Time series of DI\_EASMI during 1921–2010 (black line) and 3-year leading DI\_SSTI (blue line), 4-

778 year leading DI\_BH (green line) and 5-year leading DI\_SIC (red line)



779  
 780 Fig. 6 25-year running correlation between DI\_EASMI during 1921–2010 and leading DI of predictors (**a**  
 781 BH, **b** SSTI, **c** SIC). The dotted line is at the 95% confidence level by the student’s t-test, and the effective  
 782 sample numbers are 22, 23, and 22, respectively



783

784

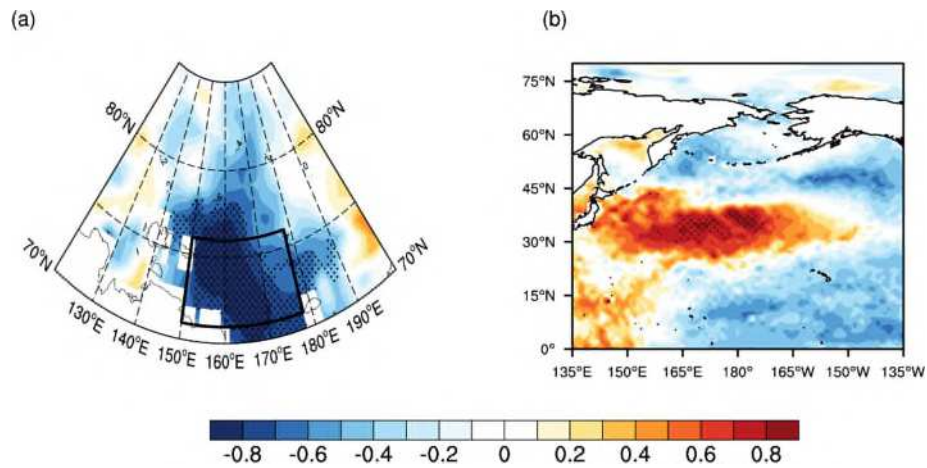
785

786

787

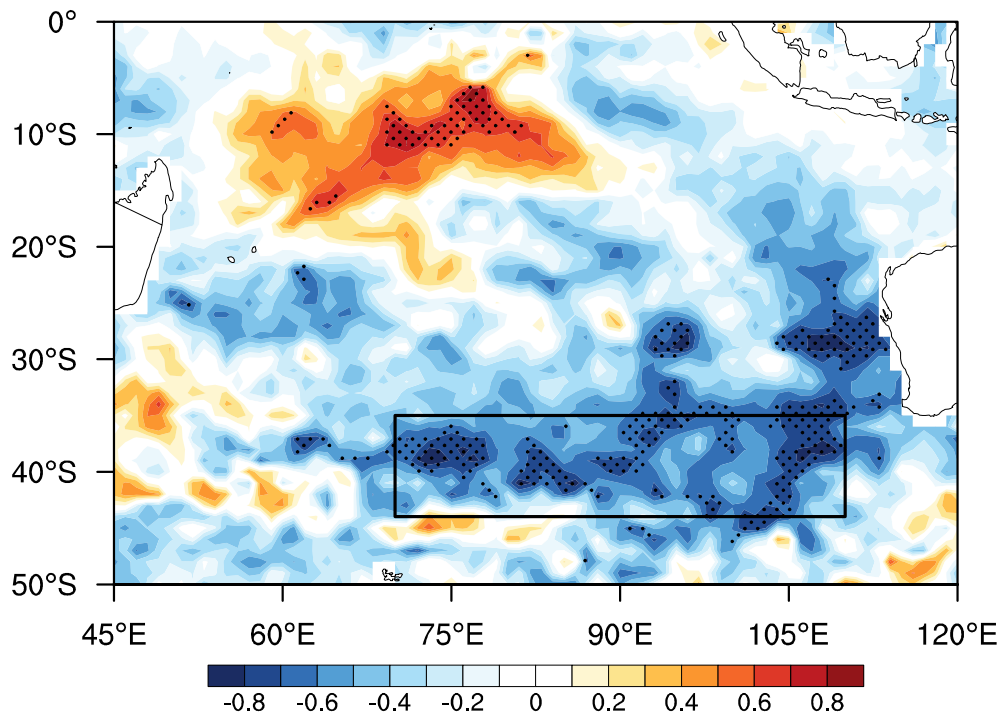
788

Fig. 7 Predictions of **a, d** DI\_EASMI and **b, e** EASMI and **c, f** the results of the moving t-test with a 10-year moving window of EASMI (**a, b, c** results of the cross validation during 1921–2010; **d, e, f** results of independent hindcast during 1980–2010; the light pink shading indicates the 95% confidence interval of the prediction. The value in the upper right corner is the correlation coefficient/MSSS between observations and predictions; the thin solid lines in **c** and **f** are significant at the 95% confidence levels)



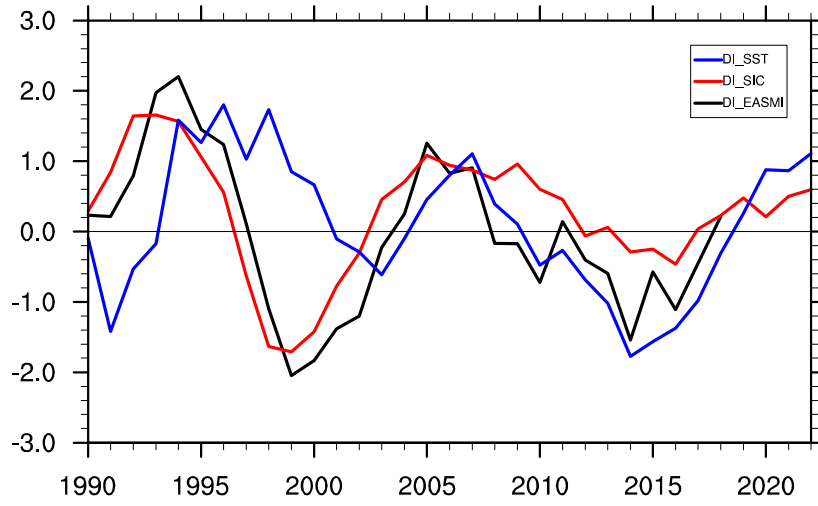
789

790 Fig. 8 **a** Correlation coefficient between DI\_EASMI during 1990–2018 and the leading 4-year summer (June  
 791 to August) DI of sea ice cover. The box indicates the key area of the predictor, and area-weighted regionally  
 792 averaged DI\_SIC (71°–76°N, 150°–178°E) is used as a predictor. **b** Correlation coefficient between summer  
 793 DI\_SIC during 1986–2014 and the spring (March to May) DI of sea surface temperature during 1990–2018.  
 794 Dotted areas indicate values significant at the 95% confidence level by the student's t-test



795

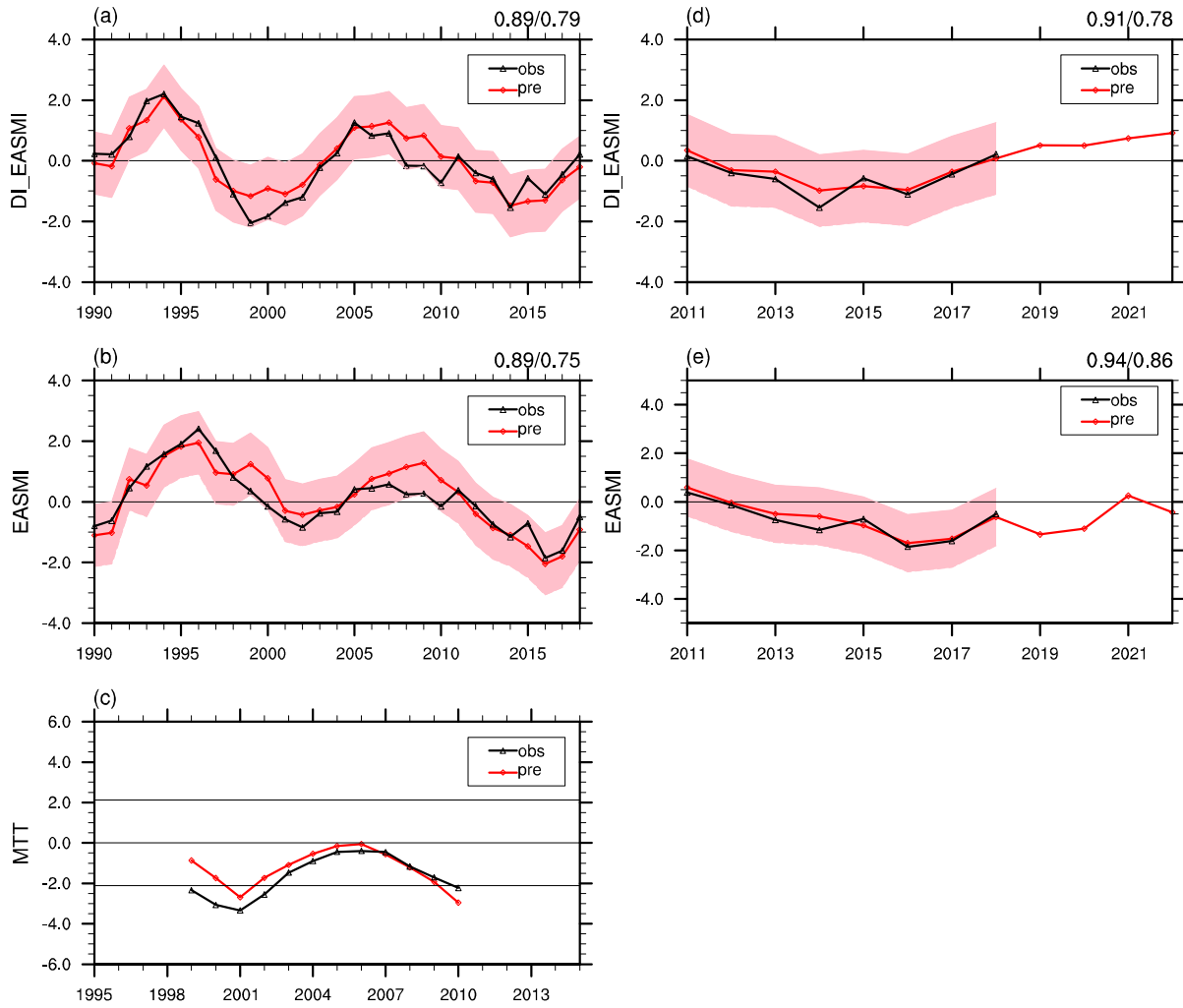
796 Fig. 9 Correlation coefficient between DI\_EASMI during 1990–2018 and the 4-year leading DI of sea  
 797 surface temperature in summer (June to August). Dotted areas indicate values significant at the 95%  
 798 confidence level by the student's t-test, and the box indicates the key area of the predictor, including DI\_SST  
 799 (35°S–44°S, 70°E–110°E)



800

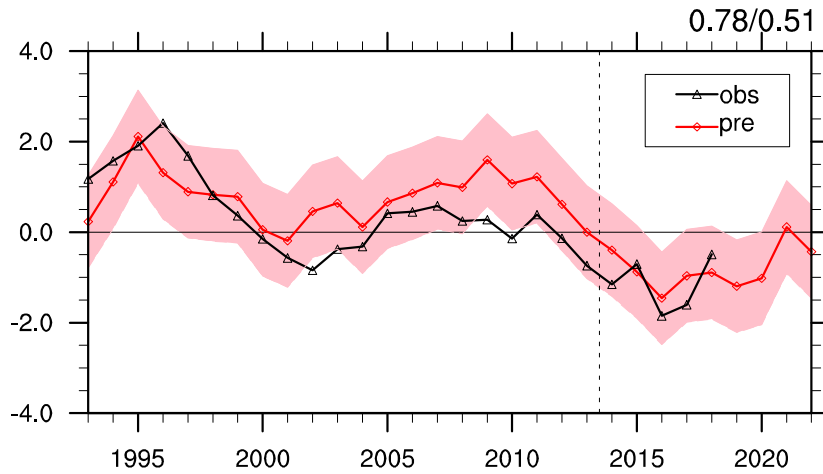
801 Fig. 10 Time series of DI\_EASMI during 1990–2018 (black line) and 4-year leading DI\_SST (blues line)

802 and DI\_SIC (red line) during 1990–2022



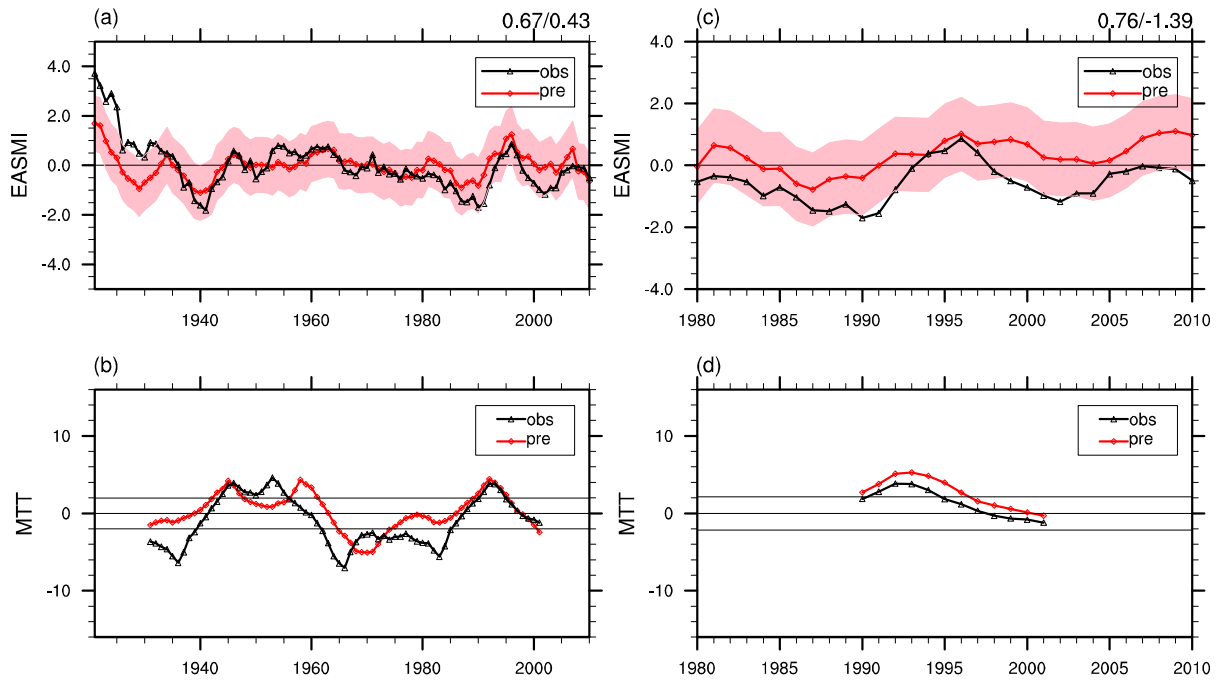
803

804 Fig. 11 Predictions of **a, d** DI\_EASMI and **b, e** EASMI and **c** the results of the moving t-test with a 9-year  
 805 moving window of EASMI (**a, b, c** results of the cross validation during 1990–2018; **d, e** results of  
 806 independent hindcast during 2011–2022; the light pink shading indicates the 95% confidence interval of the  
 807 prediction. The value in the upper right corner is the correlation coefficient/MSSS between observations and  
 808 predictions; the thin solid lines in **c** are significant at the 95% confidence levels by the student’s t-test)

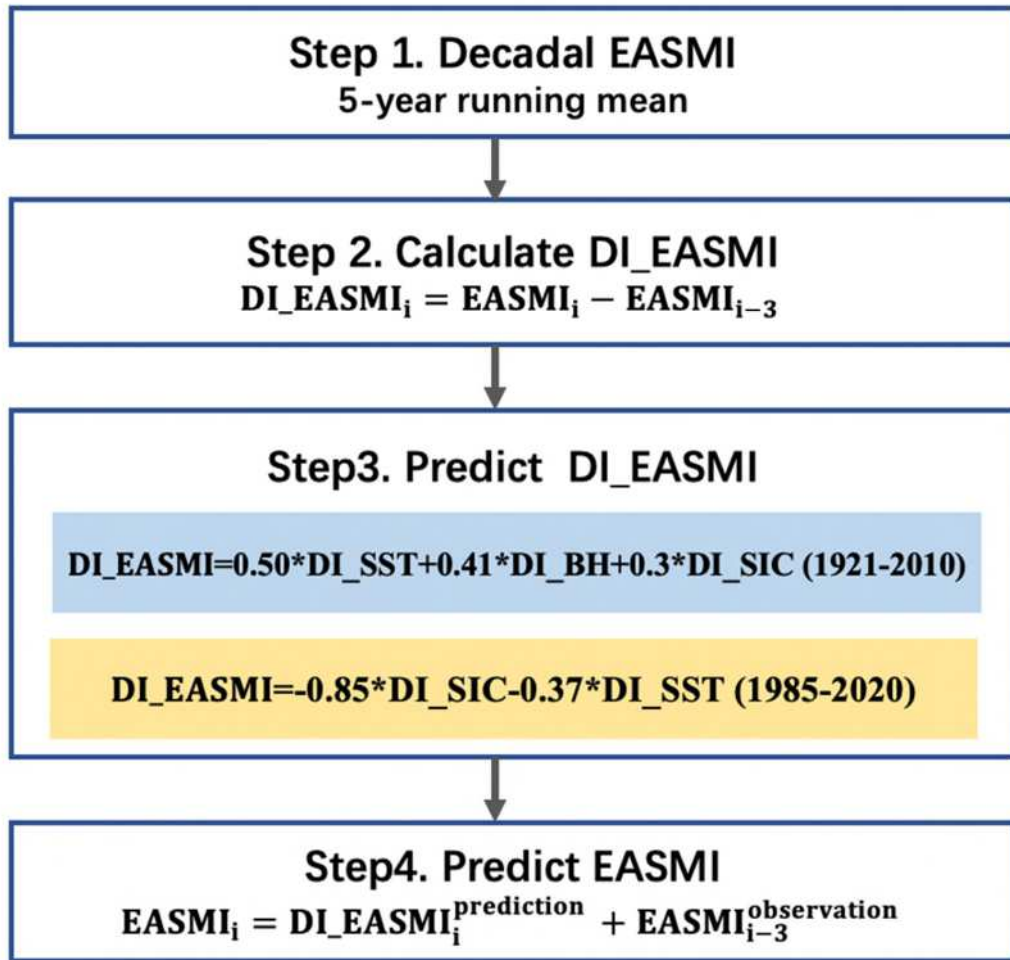


809

810 Fig. 12 Re-predictions of EASMI during 1993–2022, which is obtained by adding the predicted DI\_EASMI  
 811 from statistical model to the EASMI prediction result three years ago from decadal increment (left of the  
 812 dotted line: results of the cross validation during 1993–2013; right of the dotted line: results of the  
 813 independent hindcast during 2014–2022). The light pink shading indicates the 95% confidence interval of  
 814 the prediction. The value in the upper right corner is the correlation coefficient/MSSS between observations  
 815 and predictions



816  
 817 Fig. 13 Direct predictions of EASMI **a, c** based on statistical prediction model in the original form and **b, d**  
 818 the results of the moving t-test with a 10-year moving window (**a, c** results of the cross validation during  
 819 1921–2010; **b, d** results of independent hindcast during 1980–2010; the light pink shading indicates the 95%  
 820 confidence interval of the prediction. The value in the upper right corner is the correlation coefficient/MSSS  
 821 between observations and predictions; the thin solid lines in **b** and **d** are significant at the 95% confidence  
 822 levels by the student's t-test)



823

824 Fig. 14 Schematic diagram illustrating the process of predicting EASM using the decadal increment method

## Supplementary Files

This is a list of supplementary files associated with this preprint. Click to download.

- [Supplement.docx](#)